

Supplemental Material: Dynamical Signatures of Symmetry Broken and Liquid Phases in an $S = 1/2$ Heisenberg Antiferromagnet on the Triangular Lattice

Markus Drescher,^{1,*} Laurens Vanderstraeten,² Roderich Moessner,³ and Frank Pollmann^{1,4}

¹*Department of Physics, Technische Universität München, 85748 Garching, Germany*

²*Center for Nonlinear Phenomena and Complex Systems,
Université Libre de Bruxelles, 1050 Brussels, Belgium*

³*Max-Planck-Institut für Physik komplexer Systeme, 01187 Dresden, Germany*

⁴*Munich Center for Quantum Science and Technology (MCQST), 80799 Munich, Germany*

(Dated: November 14, 2023)

A: Spectral Functions from Dynamical Correlations

We compute the dynamical spin structure factor from time-dependent spin correlations according to equation (3) of the main text. The quantum state is represented by an MPS wrapped around a cylinder with circumference $L_y = 6$. The ground state is found via an iDMRG simulation [1] on a $L_y \times 3$ unit cell. By periodically repeating the unit cell, we can build a large system whose center site j_c is perturbed by a local \hat{S}^- operator. In the antiferromagnetically ordered phase at $J_2 = 0$, we used cylinders with $L_y = 6$ and $L_x = 51$ as well as $L_x = 126$, whereas in the QSL phase at $\frac{J_2}{J_1} = 0.125$, the system size was given by $L_y = 6$ and $L_x = 51$.

The MPO W_H time-evolution algorithm [2, 3] is suited to fully capture long-range interactions as they occur in the two-dimensional system mapped onto a cylinder. For the final large-scale tensor-network simulations, we terminated the iMPS of the ground state for the enlarged system by applying the dominant left and right eigenvector of the associated transfer matrix to the system which have been found using a power method [4]. The obtained finite MPS can be optimized at the boundaries using DMRG on a segment of a few of the outmost rings. Thus we can run the simulations on a large finite MPS with open boundary conditions in x -direction. This results in an effective speed-up of the time-evolution simulation compared to the infinite system. The bulk physics does not change.

The time-step size we used for the data presented is $\delta t = 0.04J_1$. The correlations are computed every $N_{\text{steps}} = 5$ simulation steps. We apply $U(1)$ charge conservation during the time evolution (i.e., the total S^z quantum number is conserved) [5–7]. The protocol how to compute the spin structure factor from the dynamical correlations involves several single steps: First, we can interpolate the correlation data for times between t and $t + N_{\text{steps}} \cdot \delta t$. We apply then a discrete Fourier transformation in space that yields the momentum-resolved time-dependent data. For each point in momentum space, we perform a linear prediction that extends the time series by $f_{\text{LinPre}} \cdot T_{\text{sim}}$, where T_{sim} is the total simulation time. The choice of $f_{\text{LinPre}} = 10$ has turned out to be suitable for the systems under consideration, where always

$m_{\text{LinPre}} = 20$ values of the time series have been taken into account to predict the next value. To conclude the computation, we performed a Fourier transformation of the time series convoluted with a Gaussian window function to prevent Gibb's oscillations due to the limited reachable simulation time. The Gaussian distribution was chosen to have a defined value of α at $t = T_{\text{sim}}$, i.e., the broadening is given as

$$\sigma = \sqrt{\frac{T_{\text{sim}}^2}{-2 \ln(\alpha)}}. \quad (1)$$

For the plots shown in the main text and the Supplemental Material, we chose $\alpha = 0.01$, corresponding to a Gaussian broadening of $\sigma \approx 19.8J_1$ for $T_{\text{sim}} = 60J_1$. As a result of these parameter settings, the convolution with the Gaussian function distributes the main weight to the actual simulation data whereas the linearly predicted data occurs only in the tail of the Gaussian envelope, thus avoiding a sharp cutoff of the time series and consequently Gibb's oscillations in the Fourier transform.

k_y Resolved Time Evolution.—The method above provides the dynamical correlation data for all available cuts through the full two-dimensional Brillouin zone that are accessible on an $L_y \times L_x$ -geometry (cf. Fig. 10). Since the entanglement entropy grows under time evolution of the perturbed ground state, the bond dimension χ restricts the feasible simulation times and determines the accuracy of the results. Consequently, if one separates the contributions from the different cuts in the Brillouin zone, the increasing entanglement for the corresponding momentum quantum numbers can be captured more faithfully and the overall accuracy for a given bond dimension is expected to improve.

To achieve this, we can apply a local operator with well-defined momentum $k_y(m_2) = 2\pi \frac{m_2}{L_y}$ ($m_2 \in \mathbb{Z}$) in \mathbf{b}_2 -direction instead of a single-site operator:

$$\hat{S}_{n_1}^-(k_y) = \frac{1}{\sqrt{L_y}} \sum_{j=0}^{L_y-1} e^{ij \cdot k_y} \hat{S}_{n_1 \cdot \mathbf{a}_1 + j \cdot \mathbf{a}_2}^-. \quad (2)$$

The primitive lattice vectors are $\mathbf{a}_1 = (1, 0)^T$ and $\mathbf{a}_2 = \left(\frac{1}{2}, \frac{\sqrt{3}}{2}\right)^T$ with the corresponding reciprocal lattice vec-

tors $\mathbf{b}_1 = \left(2\pi, -\frac{2\pi}{\sqrt{3}}\right)^T$ and $\mathbf{b}_2 = \left(0, \frac{4\pi}{\sqrt{3}}\right)^T$. The time evolution can be achieved by the same techniques as before. The correlations are taken with respect to the hermitian conjugate operator

$$C_{k_y}(n'_1, n_1; t) = \langle e^{iHt} \left(\hat{S}_{n'_1}^-(k_y) \right)^\dagger e^{-iHt} \hat{S}_{n_1}^-(k_y) \rangle, \quad (3)$$

thus yielding effectively one-dimensional correlations in the x -coordinate. Fig. 1 shows the time-evolved bipartite entanglement entropy at the center of the system (upper row) and the dynamical correlation function (bottom row) for a momentum-resolved simulation with $k_y = 2\pi \frac{m_2}{L_y} \big|_{m_2=2}$ (left column) and for the general procedure using a single-site operator (right column) in the symmetry-broken phase at $J_2 = 0$.

As mentioned in the main text, there are two distinct sectors in the QSL phase on a $L_y = 6$ cylinder [8, 9]. The even sector is found directly by the DMRG simulation. In this sector, the entanglement spectrum on the bonds is symmetric around the total S^z quantum number $q_z = 0$. By adiabatically inserting a flux of $\theta = 2\pi$ [4], the wave function transitions into the odd sector, which results in a state whose entanglement spectrum is symmetric around $q_z = \frac{1}{2}$, indicating the existence of a spinon quasiparticle with $S^z = \pm \frac{1}{2}$ on each boundary [9]. The ground state energy in the odd sector is slightly lower and the correlations are more isotropic.

Fig. 2 shows the static structure factor from the DMRG simulation for the 120° ordered phase and the candidate quantum spin-liquid phase at $\frac{J_2}{J_1} = 0.125$. In contrast to Fig. 2 in the main text, we do not apply an interpolation scheme here. The observable features are identical. Due to the small finite cylinder circumference of $L = 6$, the data displays a structure of discrete stripes along the direction of \mathbf{b}_1 .

Figs. 3 and 4 show the dynamical spin structure factors for $J_2 = 0$ and $\frac{J_2}{J_1} = 0.125$ in a linear and a logarithmic color scale for all available cuts through the Brillouin zone for various bond dimensions. The simulation resolving the gapless Goldstone mode at the K point has turned out to be numerically particularly challenging. Therefore, the best converged data presented has been obtained from a k_y resolved time evolution with $m_2 = 2$. Note that the maximum spectral intensity has been bound by a maximum value to reveal lower-intensity features of the excitation spectrum. The maximum spectral intensity shown in each subplot has been normalized to one. No cutoff has been applied for $J_2 = 0$ along $M' - M$ and $\Gamma - M''$ and in the QSL phase along $M' - M$. To ensure that the data has converged, we ran multiple simulations with different maximal bond dimensions χ , time step sizes δt and system sizes L_x . L_x and χ strongly restrict the reliably reachable simulation times. We performed a time evolution up to $T_{\text{sim}} = 60J_1$ with bond dimensions up to $\chi = 1500$ and $\chi = 2000$ in the case

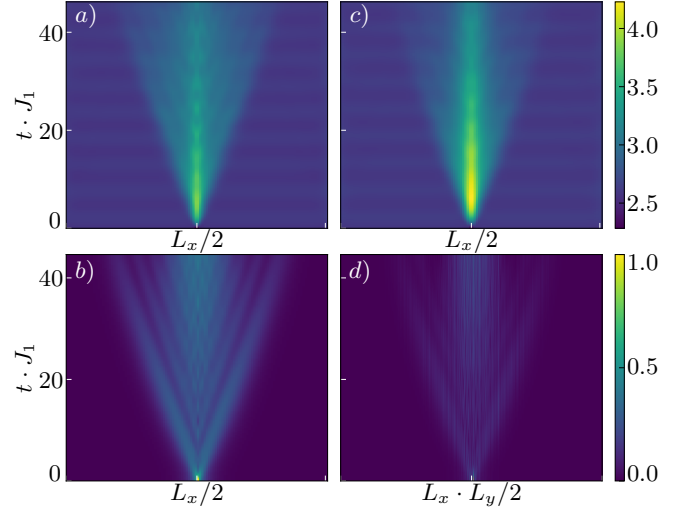


FIG. 1. a) Entanglement cone and b) correlation spreading after perturbing the ground state at $J_2 = 0$ with a momentum-resolved operator versus the corresponding quantities in the right column for a single-site perturbation operator $S_{j_c}^-$. Note that in d), the spatial index runs spirallike through the whole system, not only along the x -direction as in the other cases. The simulations were performed on a 6×126 cylinder with bond dimensions $\chi = 1300$ and $\chi = 1500$ for the momentum-resolved operator and the single-site operator respectively and time-step size $\delta t/J_1 = 0.04$.

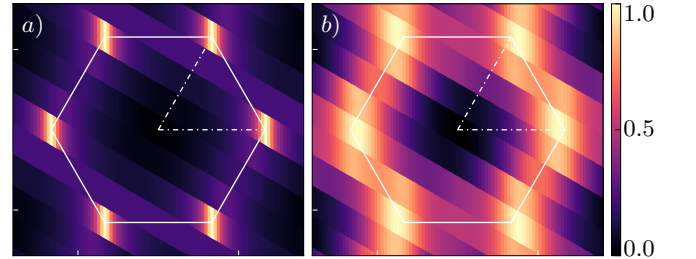


FIG. 2. Static structure factor on a cylinder with dimensions 6×51 in a) the 120° ordered phase and b) in the candidate spin-liquid phase. We show the same data as in Fig. 2 in the main text, but without using an interpolation scheme along the \mathbf{a}_2 direction of the lattice (the circumference of our cylinder).

of $J_2 = 0$ and $\frac{J_2}{J_1} = 0.125$ respectively. From comparing the first two rows in both Fig. 3 and 4, we can evaluate the convergence of the spectral function since the respective simulations have been run for different bond dimensions. Remarkably, Fig. 3e) shows a smoother and hence better converged dispersion around the high concentration of spectral weight at the K -point than Fig. 3d) even though for the latter, we used $\chi = 1500$ and for the former $\chi = 1300$. Fig. 3e), however, was obtained using the k_y momentum-resolved algorithm.

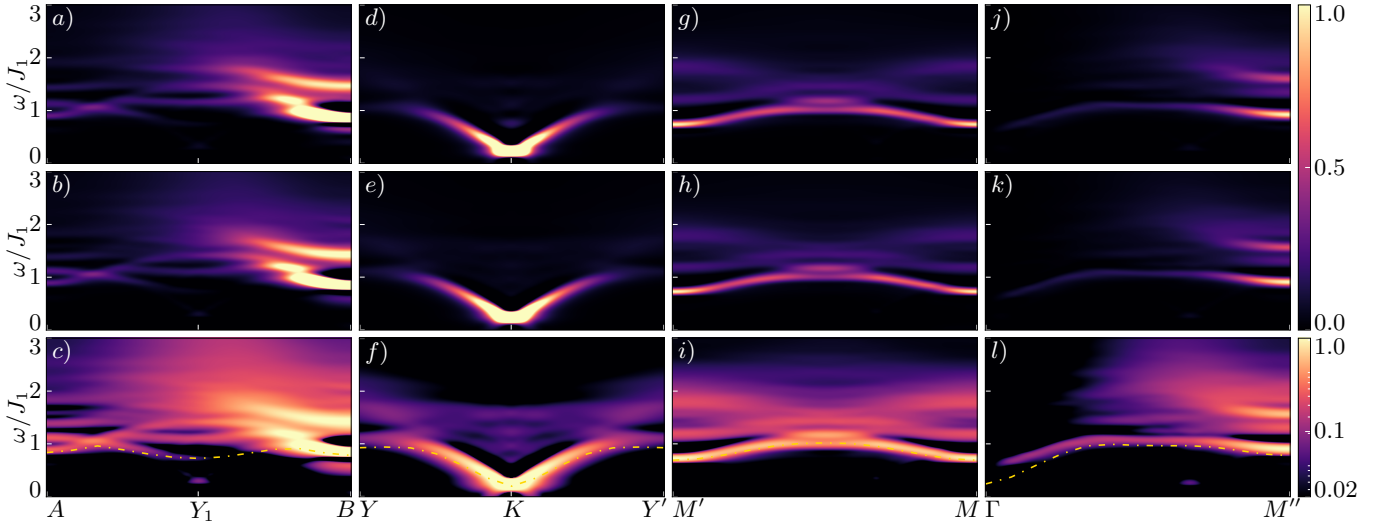


FIG. 3. Convergence of the dynamical spin structure factor $S^{+-}(\mathbf{k}, \omega)$ in the 120° ordered phase at $J_2 = 0$. The simulations have been done on a cylinder of size 6×126 . We used bond dimensions $\chi = 1200$ [a), g) and j)] and $\chi = 1500$ [b), d), h) and k)]. For Fig. e), we applied the k_y resolved time-evolution algorithm with $\chi = 1300$. The two upper rows are plotted with a linear color scale. The third row shows the same data as the second, but in a logarithmic scale. The colormap is normalized to the maximum intensity shown in the single subfigure. The golden dot-dashed line denotes the energy of the lowest branch as obtained from the quasiparticle ansatz.

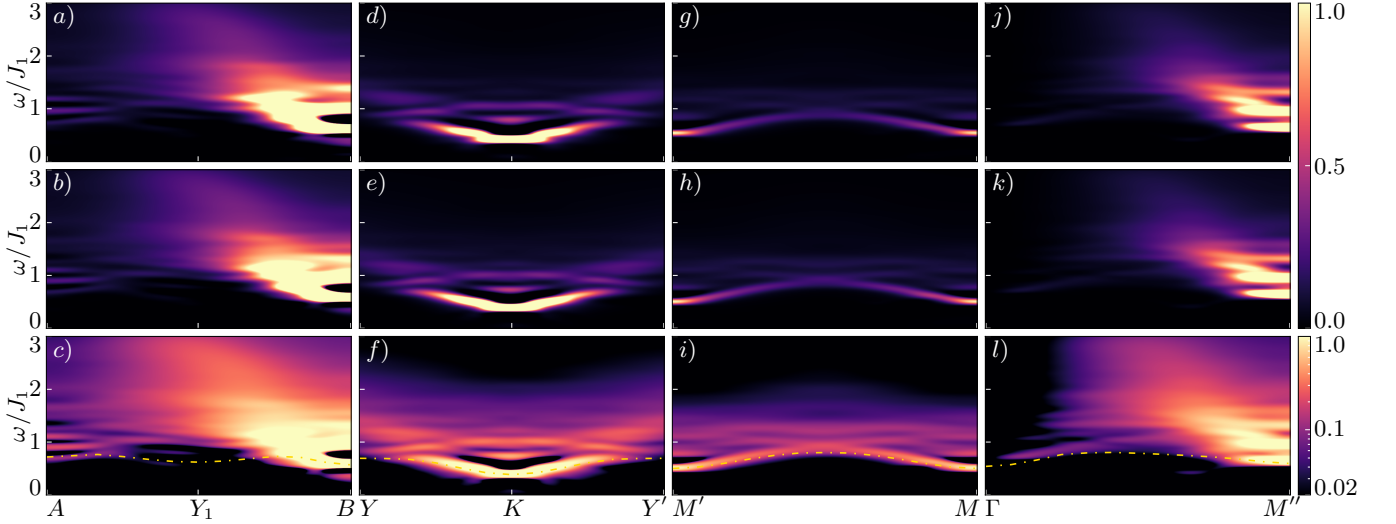


FIG. 4. Convergence of the dynamical spin structure factor $S^{+-}(\mathbf{k}, \omega)$ in the QSL phase at $J_2/J_1 = 0.125$. The simulations have been done on a cylinder of size 6×51 . The first row shows data for a bond dimension of $\chi = 1500$, the second for $\chi = 2000$. The third row displays the same data as the second, but plotted with a logarithmic color scale instead of a linear one. The colormap is normalized to the maximum intensity shown in the single subfigure. As before, the golden dot-dashed line denotes the energy of the lowest branch as obtained from the quasiparticle ansatz.

B: Quasiparticle Ansatz

In our work, we have also used the MPS quasiparticle ansatz [10, 11], which allows us to target momentum states on top of an infinite MPS ground state directly in the thermodynamic limit. Here we use the adaptation to cylinder geometries where the k_y momentum is used as an approximate quantum number [12]. In ad-

dition, we have used $SU(2)$ quantum numbers in the MPS ground state and quasiparticle ansatz, allowing us to target triplet excitations explicitly. The optimization of the variational energy of a quasiparticle ansatz for given momenta (k_x, k_y) gives us the energy dispersion of the lowest-lying excitations in the system. The variational wavefunction also allows us to compute the spectral weights of these states such that we can compute

their contributions to the spectral function.

Let us start from the definition of the spectral function

$$S(\mathbf{k}, \omega) = \sum_{\alpha} \int dt e^{i\omega t} \langle \Psi_0 | e^{iHt} (\hat{S}_{\mathbf{k}}^{\alpha})^{\dagger} e^{-iHt} \hat{S}_{\mathbf{k}}^{\alpha} | \Psi_0 \rangle, \quad (4)$$

where we use the sum of the three spin components α such that we do not break $SU(2)$ symmetry. We have defined a momentum operator formally as

$$\hat{S}_{\mathbf{k}}^{\alpha} = \frac{1}{\sqrt{L_x L_y}} \sum_{\mathbf{r}} e^{i\mathbf{k} \cdot \mathbf{r}} \hat{S}_{\mathbf{r}}^{\alpha} \quad (5)$$

in the limit $L_x \rightarrow \infty$ of an infinitely long cylinder. We can now project the spectral function on the first low-lying excitations, resulting in

$$S_{\text{low}}(\mathbf{k}, \omega) = \sum_{\gamma} \int dt e^{i\omega t} e^{-i\Delta_{\gamma}(\mathbf{k})t} \sum_{\alpha} |\langle \Phi_{\mathbf{k}}^{\gamma} | \hat{S}_{\mathbf{k}}^{\alpha} | \Psi_0 \rangle|^2 \quad (6)$$

$$= \sum_{\gamma} \sum_{\alpha} |\langle \Phi_{\mathbf{k}}^{\gamma} | \hat{S}_{\mathbf{k}}^{\alpha} | \Psi_0 \rangle|^2 2\pi\delta(\omega - \Delta_{\gamma}(\mathbf{k})) \quad (7)$$

where γ labels the excited states with excitation energy $\Delta_{\gamma}(\mathbf{k})$. In order to plot this projected spectral function, we convolute the delta signal with a Gaussian broadening

$$2\pi\delta(\omega) \rightarrow \frac{\sqrt{2\pi}}{\sigma} \exp\left(-\frac{\omega^2}{2\sigma^2}\right) \quad (8)$$

Note that along the momentum cut $M'-M$ through the Brillouin zone [Fig. 3f], the lowest branch is made up out of two separate but almost degenerate excitations. Therefore, we plot the averaged energy and the added spectral weight [Fig. 5c].

C: Integrated Spectral Weight

The energy dispersion for the lowest branch obtained using the two different approaches described in the two preceding sections show good agreement for the accessible momenta in the Brillouin zone (cf. Fig. 3). One specific feature is the repulsion of the magnon branch between A and B in the ordered phase as discussed in the main text. One prominent characteristic of this renormalized branch is the almost vanishing spectral weight near the energetic minimum. To verify the reliability of the two methods, we compare the integrated spectral weight for the lowest branch obtained from the dynamical correlation function and the quasiparticle ansatz.

The latter allows us to access the variational wavefunction for the lowest-lying excitations, thus enabling us to compute the integrated spectral weight of the corresponding excitation modes. From the Lehmann representation of equation (7), we find for the integrated spectral weight of the lowest-energy excitations, denoted by the wavefunctions $|\Phi_{\mathbf{k}}^{\gamma}\rangle$:

$$\int d\omega S_{\text{low}}(\mathbf{k}, \omega) = 2\pi \sum_{\gamma} \sum_{\alpha} |\langle \Phi_{\mathbf{k}}^{\gamma} | \hat{S}_{\mathbf{k}}^{\alpha} | \Psi_0 \rangle|^2. \quad (9)$$

Due to the translation invariance of the ground state, the spectral function in equation (3) of the main text is equivalent to

$$S^{+-}(\mathbf{k}, \omega) = \frac{1}{N} \int dt \sum_{i,j} e^{i\omega t - i\mathbf{k} \cdot (\mathbf{r}_i - \mathbf{r}_j)} \langle e^{iHt} \hat{S}_i^{+} e^{-iHt} \hat{S}_j^{-} \rangle, \quad (10)$$

where $N = L_y \cdot L_x$ is the number of sites. In the Lehmann representation, this reads

$$S^{+-}(\mathbf{k}, \omega) = \sum_n |\langle n | \hat{S}_{\mathbf{k}}^{-} | \Psi_0 \rangle|^2 2\pi\delta(\omega + E_0 - E_n). \quad (11)$$

$\{|n\rangle\}$ denotes the set of energy eigenstates with energies E_n and E_0 is the ground state energy. For an $SU(2)$ invariant state, it holds that

$$\sum_n |\langle n | \hat{S}_{\mathbf{k}}^{\pm} | \Psi_0 \rangle|^2 = \sum_n \left[|\langle n | \hat{S}_{\mathbf{k}}^x | \Psi_0 \rangle|^2 + |\langle n | \hat{S}_{\mathbf{k}}^y | \Psi_0 \rangle|^2 \right]. \quad (12)$$

Hence, we can establish the following relation for the integrated spectral weight for an $SU(2)$ symmetric ground state:

$$\sum_n \sum_{\alpha} |\langle \Phi_{\mathbf{k}}^n | \hat{S}_{\mathbf{k}}^{\alpha} | \Psi_0 \rangle|^2 = \frac{1}{2\pi} \int d\omega S(\mathbf{k}, \omega) \quad (13)$$

$$= \chi(\mathbf{k}) \quad (14)$$

$$= \frac{3}{2} \sum_n |\langle n | \hat{S}_{\mathbf{k}}^{-} | \Psi_0 \rangle|^2 \quad (15)$$

$$= \frac{3}{4\pi} \int d\omega S^{+-}(\mathbf{k}, \omega). \quad (16)$$

Note that the total integrated spectral weight is identical to the static spin structure factor in equation (2) of the main text. Hence, the spectral weight for the lowest-energy excitations that we obtain from the quasiparticle ansatz is related to the integrated spectral weight from the dynamical structure factor as computed above via

$$\sum_{\gamma} \sum_{\alpha} |\langle \Phi_{\mathbf{k}}^{\gamma} | \hat{S}_{\mathbf{k}}^{\alpha} | \Psi_0 \rangle|^2 = \frac{3}{4\pi} \int d\omega S_{\text{low}}^{+-}(\mathbf{k}, \omega). \quad (17)$$

Here, we integrate only over the lowest-excitation branch in the spectral function for a given momentum \mathbf{k} .

Fig. 5 shows the spectral weights obtained from the two distinct methods for the lowest-energy branch on the different lines through the Brillouin zone as displayed in Fig. 3 of the main text. We observe good agreement between the absolute numbers, which underlines the validity of the results.

D: Spectral Functions in the Stripe Phase

In Fig. 6, we provide spectral data for $\frac{J_2}{J_1} = 0.55$ in the stripe-ordered phase. As mentioned in the main text, the DMRG algorithm with $U(1)$ charge conservation we use

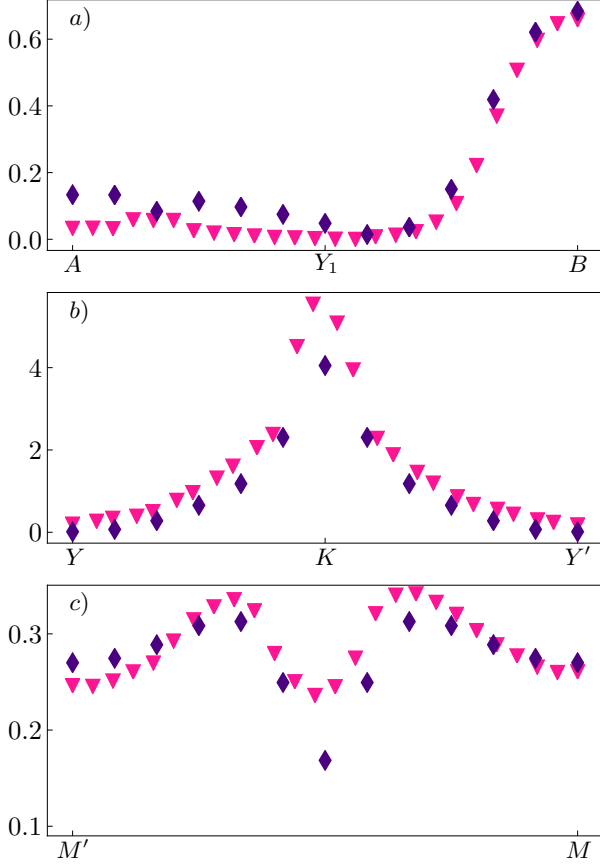


FIG. 5. Comparison of the integrated spectral weight for the lowest-energy excitation $\sum_{\gamma} \sum_{\alpha} |\langle \Phi_{\mathbf{k}}^{\gamma} | \hat{S}_{\mathbf{k}}^{\alpha} | \Psi_0 \rangle|^2$ (cf. equation (17)) from the quasiparticle ansatz (blue diamonds) and the full spectral function (red triangles) along the different lines in the Brillouin zone in Fig. 3 (main text) for the symmetry broken phase at $J_2 = 0$.

here to find the ground state chooses a certain symmetry-broken state as the ground state. The numerically determined ground state is hence not a superposition of all possible orientations of the stripe-ordered state and its static structure factor exhibits a peak at M' , but not at M .

We observe that a gapless Goldstone mode develops at M' as expected. Overall, deep in the symmetry-broken phase, one can observe clear magnon modes with well-defined dispersions. They agree well with the results from linear spin-wave theory as shown in Fig. 6. When plotting the linear spin-wave dispersion, we added a finite size gap to the energy as it develops in the system under consideration. The gap has been extracted at the maximum of the spectral weight at momentum M' where the Goldstone mode becomes gapless. We found a numerical value of

$$\Delta E_{\text{finite-size}} \left(\frac{J_2}{J_1} = 0.55 \right) \approx 0.169 J_1. \quad (18)$$

In comparison, the finite size gap as obtained from the quasiparticle ansatz at the expected gapless K point for the Goldstone in the 120° ordered phase at $J_2 = 0$ was found to be

$$\Delta E_{\text{finite-size}} (J_2 = 0) \approx 0.191 J_1. \quad (19)$$

From linear spin-wave theory, we expect an accidental zero mode at the edge-centers M and M' where no Goldstone modes are located. In the light of equation (18), however, our results indicate a clear finite gap that exceeds the finite-size gap of the system [see Figs. 6c) and d)]. This is in accordance with the settled insight that quantum fluctuations in Heisenberg models gap out the accidental zero modes [13–15].

E: Spin-Wave Theory

Linear Spin-Wave Theory in the 120° Ordered Phase

We calculated the magnon dispersion for the nearest-neighbor Heisenberg model on the triangular lattice in linear spin-wave theory [16–20] to be compared with our numerical DMRG results. Starting from the Hamiltonian

$$H_{\text{nn}} = J_1 \sum_{\langle ij \rangle} (S_i^x S_j^x + S_i^y S_j^y + S_i^z S_j^z), \quad (20)$$

we first perform a local rotation of the coordinate system in order to align the spins in the 120° state locally with the rotated z' -axis (spins are assumed to lie in the x - z -plane):

$$\begin{aligned} S_i^z &= \cos(\theta_i) S_i^{z'} - \sin(\theta_i) S_i^{x'} \\ S_i^x &= \sin(\theta_i) S_i^{z'} + \cos(\theta_i) S_i^{x'}. \end{aligned} \quad (21)$$

This yields

$$\begin{aligned} H_{\text{nn}} &= J_1 \sum_{\langle ij \rangle} \left[S_i^{y'} S_j^{y'} + \cos(\theta_i - \theta_j) \left[S_i^{z'} S_j^{z'} + S_i^{x'} S_j^{x'} \right] \right. \\ &\quad \left. + \sin(\theta_i - \theta_j) \left[S_i^{z'} S_j^{x'} - S_i^{x'} S_j^{z'} \right] \right] \end{aligned} \quad (22)$$

Applying the Holstein-Primakoff transformation $S_i^{z'} = S - a_i^\dagger a_i$ and $S_i^+ = \sqrt{2S - a_i^\dagger a_i} a_i$, we obtain in leading order

$$H_{\text{nn}} = H_0 + H_2 \quad (23)$$

with

$$H_0 = -\frac{3}{2} J_1 S^2 N \quad (24)$$

and the quadratic term

$$\begin{aligned} H_2 &= J_1 S \sum_{\mathbf{r}} \sum_{\delta} \left[-\frac{3}{4} [a_{\mathbf{r}} a_{\mathbf{r}+\delta} + a_{\mathbf{r}+\delta}^\dagger a_{\mathbf{r}}^\dagger] \right. \\ &\quad \left. + \frac{1}{4} [a_{\mathbf{r}+\delta}^\dagger a_{\mathbf{r}} + a_{\mathbf{r}}^\dagger a_{\mathbf{r}+\delta}] + \frac{1}{2} [a_{\mathbf{r}}^\dagger a_{\mathbf{r}} + a_{\mathbf{r}+\delta}^\dagger a_{\mathbf{r}+\delta}] \right], \end{aligned} \quad (25)$$

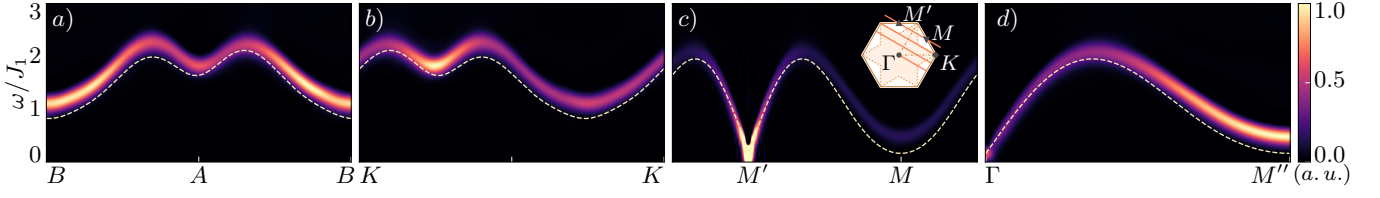


FIG. 6. Dynamical spin structure factor $S^{+-}(\mathbf{k}, \omega)$ in the stripe-ordered phase at $\frac{J_2}{J_1} = 0.55$. The simulations have been done on a cylinder of size 6×126 with bond dimensions $\chi = 800$. The dashed line denotes the dispersion from linear spin-wave theory (cf. Sec. **Linear Spin-Wave Theory in the Stripe-Ordered Phase** in this Supplemental Material).

where $\boldsymbol{\delta} = \mathbf{a}_1, \mathbf{a}_2, \mathbf{a}_3$ sums over half of the neighboring sites. The lattice translation vectors are $\mathbf{a}_1 = (1, 0)^T$, $\mathbf{a}_2 = (\frac{1}{2}, \frac{\sqrt{3}}{2})^T$ and $\mathbf{a}_3 = \mathbf{a}_1 - \mathbf{a}_2$. Moreover, we used that for nearest-neighbor pairs, $\cos(\theta_i - \theta_j) = -\frac{1}{2}$ holds. Fourier transforming this expression results in

$$H_2 = \sum_{\mathbf{k}} \left[A_{\mathbf{k}} a_{\mathbf{k}}^\dagger a_{\mathbf{k}} - \frac{1}{2} B_{\mathbf{k}} [a_{\mathbf{k}}^\dagger a_{-\mathbf{k}}^\dagger + a_{-\mathbf{k}} a_{\mathbf{k}}] \right] \quad (26)$$

with $A_{\mathbf{k}} = 3J_1 S (1 + \frac{1}{2} \gamma_{\mathbf{k}})$, $B_{\mathbf{k}} = \frac{9}{2} J_1 S \gamma_{\mathbf{k}}$ and

$$\gamma_{\mathbf{k}} = \frac{1}{6} \sum_{\boldsymbol{\delta}} (e^{i\mathbf{k} \cdot \boldsymbol{\delta}} + e^{-i\mathbf{k} \cdot \boldsymbol{\delta}}) \quad (27)$$

$$= \frac{1}{3} \left[\cos(k_x) + 2 \cos\left(\frac{k_x}{2}\right) \cos\left(k_y \frac{\sqrt{3}}{2}\right) \right]. \quad (28)$$

For $\mathbf{k} \neq \mathbf{0}, \mathbf{K}, \mathbf{K}'$, this Hamiltonian can be diagonalized via a Bogoliubov transformation $a_{\mathbf{k}} = u_{\mathbf{k}} b_{\mathbf{k}} + v_{\mathbf{k}} b_{-\mathbf{k}}^\dagger$ with the coefficients being given as

$$u_{\mathbf{k}} = \left(\frac{A_{\mathbf{k}} + \varepsilon_{\mathbf{k}}}{2\varepsilon_{\mathbf{k}}} \right)^{\frac{1}{2}} \quad (29)$$

$$v_{\mathbf{k}} = \text{sgn}(B_{\mathbf{k}}) \left(\frac{A_{\mathbf{k}} - \varepsilon_{\mathbf{k}}}{2\varepsilon_{\mathbf{k}}} \right)^{\frac{1}{2}}. \quad (30)$$

and

$$\varepsilon_{\mathbf{k}} = \sqrt{A_{\mathbf{k}}^2 - B_{\mathbf{k}}^2} = 3J_1 S \sqrt{(1 - \gamma_{\mathbf{k}})(1 + 2\gamma_{\mathbf{k}})}. \quad (31)$$

This leads to the expression

$$H_2 = \sum_{\mathbf{k}} \left[\varepsilon_{\mathbf{k}} \left(b_{\mathbf{k}}^\dagger b_{\mathbf{k}} + \frac{1}{2} \right) - \frac{A_{\mathbf{k}}}{2} \right] \quad (32)$$

(note that $\varepsilon_{\mathbf{k}}$ vanishes for $\mathbf{k} = \mathbf{0}, \mathbf{K}, \mathbf{K}'$). We finally end up with the result [20]

$$H_{\text{nn}} = -\frac{3}{2} J_1 N S(S+1) + \sum_{\mathbf{k}} \varepsilon_{\mathbf{k}} \left(b_{\mathbf{k}}^\dagger b_{\mathbf{k}} + \frac{1}{2} \right), \quad (33)$$

where we used the identity $\sum_{\mathbf{k}} (1 + \frac{\gamma_{\mathbf{k}}}{2}) = L_y \cdot L_x \equiv N$.

Static Structure Factor.—We need to calculate the correlations between different sites \mathbf{r} and \mathbf{r}' on the lattice to

compute the static structure factor $\chi(\mathbf{q})$ in (2) of the main text. For the classical 120° Néel state we find

$$\langle \mathbf{S}_{\mathbf{r}} \cdot \mathbf{S}_{\mathbf{r}'} \rangle_{\text{class}} = \begin{cases} \frac{3}{4} & \text{if } \mathbf{r} = \mathbf{r}' \\ \frac{1}{4} & \text{if } \mathbf{r}, \mathbf{r}' \text{ on the same sublattice} \\ -\frac{1}{8} & \text{if } \mathbf{r}, \mathbf{r}' \text{ on different sublattices} \end{cases}$$

We can treat quantum fluctuations within linear spin-wave theory. The spin components on site i are given in terms of the bosonic operators as

$$S_i^{z'} = S - a_i^\dagger a_i \quad (34)$$

$$S_i^{x'} = \sqrt{\frac{S}{2}} (a_i + a_i^\dagger) \quad (35)$$

$$S_i^{y'} = \frac{1}{i} \sqrt{\frac{S}{2}} (a_i - a_i^\dagger). \quad (36)$$

We find the following correlations

$$\langle S_{\mathbf{r}}^y \cdot S_{\mathbf{r}'}^y \rangle = \frac{S}{2N} \sum_{\mathbf{k}}' \sqrt{\frac{A_{\mathbf{k}} - B_{\mathbf{k}}}{A_{\mathbf{k}} + B_{\mathbf{k}}}} e^{i\mathbf{k} \cdot (\mathbf{r} - \mathbf{r}')} \quad (37)$$

$$\langle S_{\mathbf{r}}^x \cdot S_{\mathbf{r}'}^x \rangle = \frac{S}{2N} \cos(\theta_{\mathbf{r} - \mathbf{r}'}) \sum_{\mathbf{k}}' \sqrt{\frac{A_{\mathbf{k}} + B_{\mathbf{k}}}{A_{\mathbf{k}} - B_{\mathbf{k}}}} e^{i\mathbf{k} \cdot (\mathbf{r} - \mathbf{r}')} \quad (38)$$

$$\begin{aligned} \langle S_{\mathbf{r}}^z \cdot S_{\mathbf{r}'}^z \rangle = & \left\{ S^2 - 2 \frac{S}{N} \sum_{\mathbf{k}}' v_{\mathbf{k}}^2 + \frac{1}{N^2} \left(\sum_{\mathbf{k}}' v_{\mathbf{k}}^2 \right)^2 \right. \\ & + \frac{1}{N^2} \left(\sum_{\mathbf{k}}' u_{\mathbf{k}} v_{\mathbf{k}} e^{i\mathbf{k} \cdot (\mathbf{r} - \mathbf{r}')} \right)^2 \\ & \left. + \frac{1}{N^2} \sum_{\mathbf{k}}' \sum_{\mathbf{k}'}' v_{\mathbf{k}}^2 u_{\mathbf{k}'} e^{i(\mathbf{k} - \mathbf{k}') \cdot (\mathbf{r} - \mathbf{r}')} \right\} \cos(\theta_{\mathbf{r} - \mathbf{r}'} \end{aligned} \quad (39)$$

with the angular contribution being given as $\cos(\theta_{\mathbf{r} - \mathbf{r}'}) = \cos(\frac{2\pi}{3}(n_1 - n_1' - (n_2 - n_2')))$ for $\mathbf{r}^{(i)} = n_1^{(i)} \mathbf{a}_1 + n_2^{(i)} \mathbf{a}_2$. The primed sums denote momentum sums over all momenta in the Brillouin zone excluding the gapless Goldstone modes at $\mathbf{0}, \mathbf{K}$ and \mathbf{K}' . The momenta can be written as $\mathbf{k} = \frac{m_1}{L_x} \mathbf{b}_1 + \frac{m_2}{L_y} \mathbf{b}_2$ ($m_i \in \mathbb{Z}$). Note that the corners of the Brillouin zone \mathbf{K} and \mathbf{K}' are included if and only if L_x and L_y are multiples of 3.

Linear Spin-Wave Theory in the Stripe-Ordered Phase

We can apply a similar formalism as in the previous paragraph to obtain the magnon dispersion resulting from lowest-order spin-wave theory in the stripe-ordered phase at $\frac{J_2}{J_1} = 0.55$ (cf. Fig. 6). The standard approach for an antiferromagnetic ground state introduces two different kinds of bosonic operators on the sublattices of the system with opposite spin orientation [21, 22]. We want to apply a different approach in analogy to the one presented above by locally rotating the reference frame. We consider the full Hamiltonian with nearest- and next-nearest-neighbor interaction:

$$H = J_1 \sum_{\langle ij \rangle} (S_i^x S_j^x + S_i^y S_j^y + S_i^z S_j^z) + J_2 \sum_{\langle\langle ij \rangle\rangle} (S_i^x S_j^x + S_i^y S_j^y + S_i^z S_j^z) \quad (40)$$

We rotate the local frame according to equation (21) by an angle of π . The orientation of the spins in the ground state hereby alternates when going into the direction of \mathbf{a}_2 . This assumption can be verified from the numerical ground state found by DMRG at the coupling $\frac{J_2}{J_1} = 0.55$.

The nearest-neighbor pairs are given for each site as before by $\delta_{nn}^i = \mathbf{a}_i$, $i = 1, 2, 3$. For the next-nearest-neighbor pairs we choose $\delta_{nnn}^i = \mathbf{l}_i$ ($i = 1, 2, 3$) with

$$\begin{aligned} \mathbf{l}_1 &= 2\mathbf{a}_2 - \mathbf{a}_1 \\ \mathbf{l}_2 &= \mathbf{a}_1 + \mathbf{a}_2 \\ \mathbf{l}_3 &= 2\mathbf{a}_1 - \mathbf{a}_2. \end{aligned} \quad (41)$$

Defining $\Delta\theta(\mathbf{d}) = \theta_{\mathbf{r}} - \theta_{\mathbf{r}+\mathbf{d}}$ we obtain

$$\Delta\theta(\mathbf{a}_1) = \Delta\theta(\mathbf{l}_1) = 0 \quad (42)$$

$$\Delta\theta(\mathbf{a}_{2/3}) = \Delta\theta(\mathbf{l}_{2/3}) = \pm\pi. \quad (43)$$

resulting in $\cos(\Delta\theta) \in \{1, -1\}$ for the different cases.

After applying the standard Holstein-Primakoff transformation as introduced in the previous paragraph, the zeroth order Hamiltonian yields

$$H_0 = -S^2 (J_1 + J_2) N. \quad (44)$$

The second order contribution reads

$$\begin{aligned} H_2 &= J_1 S \sum_{\langle ij \rangle} \left\{ -\cos(\theta_i - \theta_j) (a_i^\dagger a_i + a_j^\dagger a_j) \right. \\ &\quad + (a_i a_j + a_j^\dagger a_i^\dagger) \frac{\cos(\theta_i - \theta_j) - 1}{2} \\ &\quad \left. + (a_i^\dagger a_j + a_j^\dagger a_i) \cdot \frac{\cos(\theta_i - \theta_j) + 1}{2} \right\} \\ &\quad + J_2 S \sum_{\langle\langle ij \rangle\rangle} \dots \end{aligned} \quad (45)$$

The terms for the next-nearest-neighbor contribution have the same form as the nearest-neighbor ones.

A transformation to Fourier space results in a Hamiltonian with a similar structure as in equation (26):

$$H_2 = \sum_{\mathbf{k}} \left[\tilde{A}_{\mathbf{k}} a_{\mathbf{k}}^\dagger a_{\mathbf{k}} - \frac{1}{2} [\tilde{B}_{\mathbf{k}}^* a_{\mathbf{k}}^\dagger a_{-\mathbf{k}}^\dagger + \tilde{B}_{\mathbf{k}} a_{-\mathbf{k}} a_{\mathbf{k}}] \right] \quad (46)$$

with

$$\begin{aligned} \tilde{A}_{\mathbf{k}} &= 2J_1 S [1 + \cos(\mathbf{k} \cdot \mathbf{a}_1)] \\ &\quad + 2J_2 S [1 + \cos(\mathbf{k} \cdot \mathbf{l}_1)] \end{aligned} \quad (47)$$

and

$$\begin{aligned} \tilde{B}_{\mathbf{k}} &= 2J_1 S [e^{i\mathbf{k} \cdot \mathbf{a}_2} + e^{i\mathbf{k} \cdot \mathbf{a}_3}] \\ &\quad + 2J_2 S [e^{i\mathbf{k} \cdot \mathbf{l}_2} + e^{i\mathbf{k} \cdot \mathbf{l}_3}]. \end{aligned} \quad (48)$$

One can diagonalize this Hamiltonian again via a canonical Bogoliubov transformation $a_{\mathbf{k}} = u_{\mathbf{k}} b_{\mathbf{k}} + v_{\mathbf{k}} b_{-\mathbf{k}}^\dagger$ with

$$u_{\mathbf{k}} = \left(\frac{\tilde{A}_{\mathbf{k}} + \varepsilon_{\mathbf{k}}}{2\varepsilon_{\mathbf{k}}} \right)^{\frac{1}{2}} \quad (49)$$

and

$$v_{\mathbf{k}} = \text{sgn}(\text{Re}\{\tilde{B}_{\mathbf{k}}\}) \left(\frac{\tilde{A}_{\mathbf{k}} - \varepsilon_{\mathbf{k}}}{2\varepsilon_{\mathbf{k}}} \right)^{\frac{1}{2}}, \quad (50)$$

yielding

$$H_2 = \sum_{\mathbf{k}} \left[\varepsilon_{\mathbf{k}} \left(b_{\mathbf{k}}^\dagger b_{\mathbf{k}} + \frac{1}{2} \right) - \frac{\tilde{A}_{\mathbf{k}}}{2} \right]. \quad (51)$$

The energy dispersion is given as

$$\varepsilon_{\mathbf{k}} = \sqrt{\tilde{A}_{\mathbf{k}}^2 - (\text{Re}\{\tilde{B}_{\mathbf{k}}\})^2}. \quad (52)$$

F: Mean-Field Theory for the Dirac Spin Liquid

Besides spin-wave theory, we explore parton mean-field theory [23–25] in the QSL phase to compare to our numerics. Starting from the Hamiltonian in equation (1) in the main text, one can substitute the spin operators by fermionic spinon operators $c_{i\alpha}$, $c_{i\alpha}^\dagger$ (the Greek letters run over the spin labels \uparrow, \downarrow) using the common parton construction

$$\mathbf{S}_i = \frac{1}{2} c_{i\alpha}^\dagger \boldsymbol{\sigma}_{\alpha\beta} c_{i\beta}, \quad (53)$$

where $\boldsymbol{\sigma} = (\sigma_x, \sigma_y, \sigma_z)$ contains the Pauli matrices. In order to describe the field theory for a Dirac spin liquid,

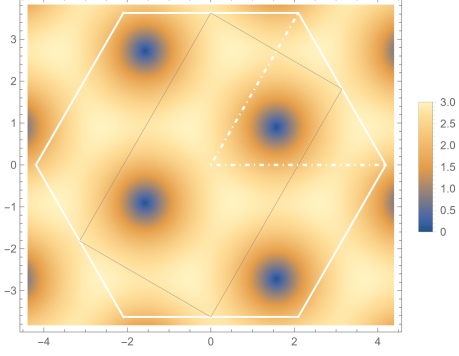


FIG. 7. Dispersion $\varepsilon_{\mathbf{k}}$ of the upper spinon band at half-filling (equation (61)) for the mean-field Dirac spin liquid. The white solid lines mark the Brillouin zone of the lattice and the thin gray line the reduced first Brillouin zone of the spinons.

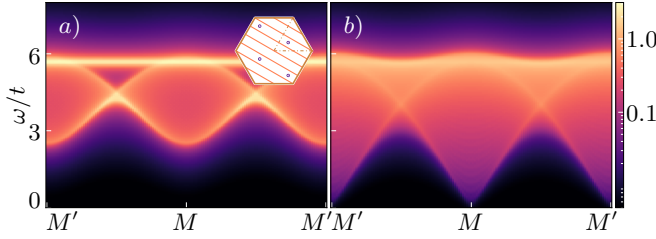


FIG. 8. Dynamical spin structure factor obtained from the mean-field parton approach for a Dirac spin liquid on a cylinder with a) $L_y = 6$ and b) $L_y = 100$ ($L_x = 142$ each). The inset in a) shows the accessible momenta on a $L_y = 6$ cylinder as orange cuts (cf. Fig. 10). The gapless Dirac points in the spinon dispersion—denoted by violet dots—are not hit, which results in a gapped dispersion.

we keep only the spin-preserving hopping terms in the mean-field expansion

$$H_{\text{MF}} = H_{\uparrow} + H_{\downarrow} \quad (54)$$

$$H_{\alpha} = - \sum_{\langle i,j \rangle} (t_{ij} c_{i\alpha}^{\dagger} c_{j\alpha} + \text{h.c.}) \quad (55)$$

and choose the phase of the hopping constant $t_{ij} = t e^{i\varphi_{ij}}$ such that the triangles of the lattice have alternatingly flux π and 0. This flux pattern requires a two-site unit cell. The Bravais vectors are then $2\mathbf{a}_1$ and \mathbf{a}_2 , whereas the reciprocal lattice vectors become $\frac{\mathbf{b}_1}{2}$ and \mathbf{b}_2 . Defining the Fourier transformation accordingly

$$c_{(n_1, n_2, \delta)\alpha} = \frac{1}{\sqrt{L_y \frac{L_x}{2}}} \sum_{\mathbf{k}} e^{i\mathbf{k} \cdot \mathbf{r}_{n_1, n_2, \delta}} c_{\mathbf{k}\delta\alpha}, \quad (56)$$

where n_1, n_2 label the unit cell and $\delta = 0, 1$ the site within the unit cell ($i \equiv (n_1, n_2, \delta)$), i.e., $\mathbf{r} = \mathbf{r}_i = (2n_1 + \delta)\mathbf{a}_1 + n_2\mathbf{a}_2$, we can bring the Hamiltonian into the form

$$H_{\alpha} = -t \sum_{\mathbf{k}} (c_{\mathbf{k}0\alpha}^{\dagger} c_{\mathbf{k}1\alpha}^{\dagger}) \mathcal{H} \begin{pmatrix} c_{\mathbf{k}0\alpha} \\ c_{\mathbf{k}1\alpha} \end{pmatrix} \quad (57)$$

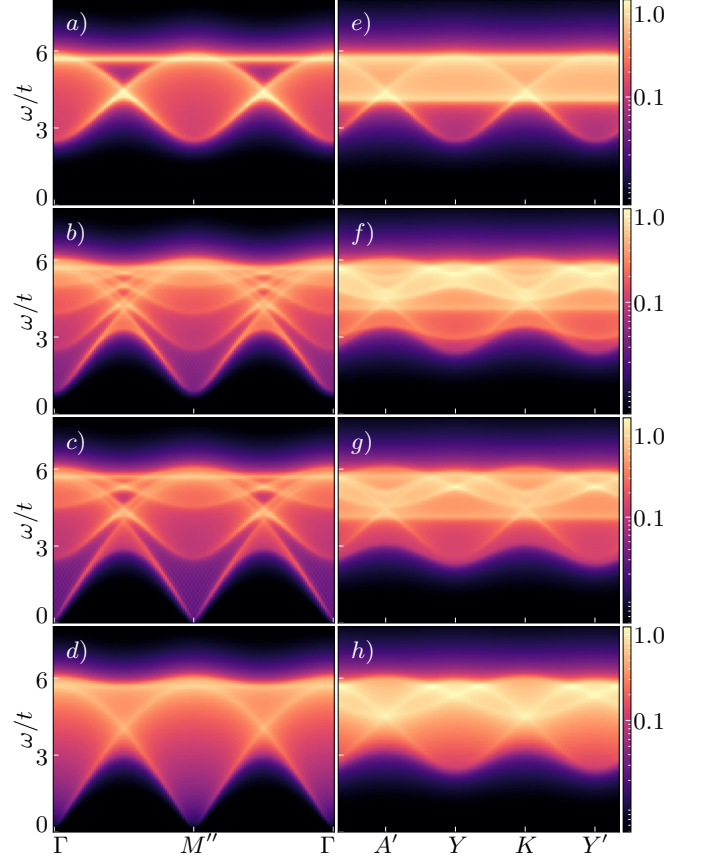


FIG. 9. Dynamical spin structure factor from the mean-field spinon theory on different cylinder circumferences: a), e) $L_y = 6$, b), f) $L_y = 9$, c), g) $L_y = 12$, d) $L_y = 100$ and h) $L_y = 96$. We apply a logarithmic color scale. See Fig. 10 for the labels of the momentum points. All calculations have been done for $L_x = 142$.

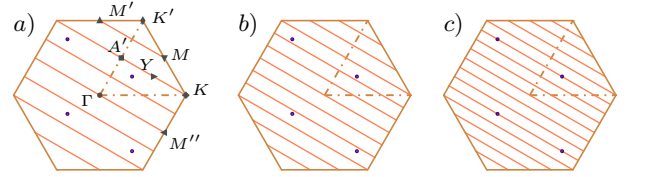


FIG. 10. Accessible momenta on cylinders with circumferences a) $L_y = 6$, b) $L_y = 9$ and c) $L_y = 12$ for $L_x \rightarrow \infty$. The violet dots denote the gapless Dirac points $\pm\mathbf{Q}$ of the spinon theory and equivalent momentum points. Note that the first Brillouin zone for the spinons has only half the size of the one for the spin model.

with

$$\mathcal{H} = \begin{pmatrix} 2 \cos(\mathbf{k} \cdot \mathbf{a}_2) & \kappa(\mathbf{k}) \\ \kappa^*(\mathbf{k}) & -2 \cos(\mathbf{k} \cdot \mathbf{a}_2) \end{pmatrix} \quad (58)$$

and

$$\kappa_{\mathbf{k}} = 2 \cos(\mathbf{k} \cdot \mathbf{a}_1) + 2i \sin(\mathbf{k} \cdot (\mathbf{a}_1 - \mathbf{a}_2)). \quad (59)$$

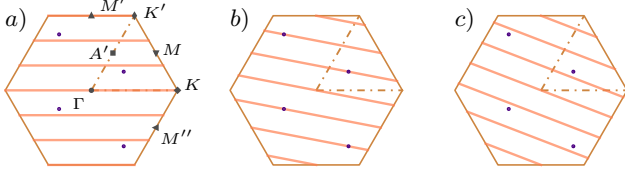


FIG. 11. Accessible momenta on cylinders with $L = 6$ for different geometries a) YC6 - 3, b) YC6 - 2 and c) YC6 - 1 for $L_x \rightarrow \infty$. The violet dots denote the gapless Dirac points $\pm \mathbf{Q}$ of the spinon theory and equivalent momentum points. The geometry YCL - n is defined in such a way that the periodicity along the circumference of the cylinder is closed by the translation $L \cdot \mathbf{a}_2 - n \cdot \mathbf{a}_1$ (cf. [4]).

The resulting energy is

$$\varepsilon_{\mathbf{k}} = \sqrt{4 \cos^2(\mathbf{k} \cdot \mathbf{a}_2) + |\kappa_{\mathbf{k}}|^2} \quad (60)$$

$$= \sqrt{2} \sqrt{3 + \cos(2k_x) - 2 \sin(k_x) \sin(\sqrt{3}k_y)}. \quad (61)$$

The diagonal Hamiltonian reads

$$H_{\alpha} = t \sum_{\mathbf{k}} \varepsilon_{\mathbf{k}} (\gamma_{\mathbf{k}1\alpha}^{\dagger} \gamma_{\mathbf{k}1\alpha} - \gamma_{\mathbf{k}0\alpha}^{\dagger} \gamma_{\mathbf{k}0\alpha}) \quad (62)$$

with the transformed operators given as

$$\gamma_{\mathbf{k}0\alpha} = \frac{\kappa^*}{\sqrt{2\varepsilon\sqrt{\varepsilon-a}}} c_{\mathbf{k}0\alpha} + \sqrt{\frac{\varepsilon-a}{2\varepsilon}} c_{\mathbf{k}1\alpha} \quad (63)$$

$$\gamma_{\mathbf{k}1\alpha} = \frac{\kappa^*}{\sqrt{2\varepsilon\sqrt{\varepsilon+a}}} c_{\mathbf{k}0\alpha} - \sqrt{\frac{\varepsilon+a}{2\varepsilon}} c_{\mathbf{k}1\alpha}. \quad (64)$$

Note that we suppressed the momentum label \mathbf{k} in $\kappa_{\mathbf{k}}$, $\varepsilon_{\mathbf{k}}$ and $a_{\mathbf{k}} = 2 \cos(\mathbf{k} \cdot \mathbf{a}_2)$. At half-filling, the lower band is occupied and Dirac cones occur at $\pm \mathbf{Q} = \pm \left(\frac{\pi}{2}, \frac{\pi}{2\sqrt{3}}\right)$. For the static spatial correlations, we find for all spin components $\beta = x, y, z$:

$$\langle S_{\mathbf{r}}^{\beta} S_{\mathbf{r}'}^{\beta} \rangle = \frac{2}{(L_x L_y)^2} \sum_{\mathbf{k}, \mathbf{q}} e^{-i(\mathbf{k}-\mathbf{q}) \cdot (\mathbf{r}-\mathbf{r}')} g_{\delta\delta'}(\mathbf{k}, \mathbf{q}). \quad (65)$$

For the sake of notational convenience, we introduced here the function

$$g_{\delta\delta'}(\mathbf{k}, \mathbf{q}) := \begin{cases} \left. \frac{|\kappa|^2}{2\varepsilon(\varepsilon-a)} \right|_{\mathbf{k}} \cdot \left. \frac{|\kappa|^2}{2\varepsilon(\varepsilon+a)} \right|_{\mathbf{q}} & \text{if } \delta = \delta' = 0 \\ \left. \frac{\varepsilon-a}{2\varepsilon} \right|_{\mathbf{k}} \cdot \left. \frac{\varepsilon+a}{2\varepsilon} \right|_{\mathbf{q}} & \text{if } \delta = \delta' = 1 \\ -\left. \frac{\kappa^*}{2\varepsilon} \right|_{\mathbf{k}} \cdot \left. \frac{\kappa}{2\varepsilon} \right|_{\mathbf{q}} & \text{if } \delta = 0, \delta' = 1 \\ -\left. \frac{\kappa}{2\varepsilon} \right|_{\mathbf{k}} \cdot \left. \frac{\kappa^*}{2\varepsilon} \right|_{\mathbf{q}} & \text{if } \delta = 1, \delta' = 0 \end{cases} \quad (66)$$

Hence, the complete static correlation function at equal time is

$$\langle \mathbf{S}_{\mathbf{r}} \cdot \mathbf{S}_{\mathbf{r}'} \rangle = 3 \cdot \langle S_{\mathbf{r}}^x S_{\mathbf{r}'}^x \rangle. \quad (67)$$

The static spin structure factor follows straightforwardly.

Dynamic Spin Structure Factor.—We can rewrite the momentum-dependent ladder operator

$$S_{\mathbf{k}}^- = \frac{1}{\sqrt{N}} \sum_{\mathbf{r}} e^{i\mathbf{k} \cdot \mathbf{r}} S_{\mathbf{r}}^- \quad (68)$$

in terms of the fermionic spinon operators:

$$S_{\mathbf{k}}^- = \sum_{\delta} \sum_{\mathbf{q}} c_{\mathbf{q}+\mathbf{k}\delta}^{\dagger} c_{\mathbf{q}\delta}. \quad (69)$$

The dynamical spin structure factor is defined as

$$S(\mathbf{k}, \omega) = \frac{1}{N} \int dt e^{i\omega t} \sum_{\mathbf{r}, \mathbf{r}'} e^{-i\mathbf{k} \cdot (\mathbf{r}-\mathbf{r}')} \langle S_{\mathbf{r}}^+(t) S_{\mathbf{r}'}^-(0) \rangle \quad (70)$$

Using the trivial time dependence of the operators $\gamma_{\mathbf{k}\delta\alpha}$, we obtain for the dynamical structure factor

$$S(\mathbf{k}, \omega) = 2\pi \sum_{\mathbf{q}} \delta(\omega - \varepsilon_{\mathbf{q}} - \varepsilon_{\mathbf{q}+\mathbf{k}}) |\langle \Phi_{\mathbf{k}}^{\mathbf{q}} | S_{\mathbf{k}}^- | \Psi_0 \rangle|^2, \quad (71)$$

where the overlap with the excited state $|\Phi_{\mathbf{k}}^{\mathbf{q}}\rangle$ with quantum number \mathbf{q} is given as

$$\begin{aligned} |\langle \Phi_{\mathbf{k}}^{\mathbf{q}} | S_{\mathbf{k}}^- | \Psi_0 \rangle|^2 &= \frac{|\kappa_{\mathbf{q}}|^2 |\kappa_{\mathbf{q}+\mathbf{k}}|^2}{4\varepsilon_{\mathbf{q}} \varepsilon_{\mathbf{q}+\mathbf{k}}} \cdot \frac{1}{\varepsilon_{\mathbf{q}} - a_{\mathbf{q}}} \cdot \frac{1}{\varepsilon_{\mathbf{q}+\mathbf{k}} + a_{\mathbf{q}+\mathbf{k}}} \\ &\quad + \frac{\varepsilon_{\mathbf{q}} - a_{\mathbf{q}}}{2\varepsilon_{\mathbf{q}}} \cdot \frac{\varepsilon_{\mathbf{q}+\mathbf{k}} + a_{\mathbf{q}+\mathbf{k}}}{2\varepsilon_{\mathbf{q}+\mathbf{k}}} \end{aligned} \quad (72)$$

Here, $|\Psi_0\rangle$ denotes the spinon ground state at half-filling. For the purpose of plotting, we model the delta-distribution in Figs. 8 and 9 as a Lorentzian

$$\delta(\omega - \varepsilon) \rightarrow \frac{\eta/\pi}{(\omega - \varepsilon)^2 + \eta^2}, \quad (73)$$

where we chose a broadening of $\eta = 0.1t$ (cf., e.g., [26]).

The resulting dynamic spin structure factor for different cylinder circumferences L_y obtained from spinon mean-field theory are shown in Fig. 9. Note that the constraint $\sum_{\alpha} c_{i\alpha}^{\dagger} c_{i\alpha} = 1$ is only satisfied on average in the mean-field treatment. (We do not apply here a Gutzwiller projector for the spectral functions shown in Figs. 8 and 9). We observe that the minima at the M points depend strongly on the choice of L_y for small cylinder circumferences. While for $L_y = 12$ it is gapless, there is a clear gap for $L_y = 6$. This is caused by the restrictions that the value of L_y imposes on the accessible momenta. For $L_y = 6$, these do not include the gapless Dirac points at $\pm \mathbf{Q}$ (cf. Fig. 10). For $L_y = 9$, momenta closer to the Dirac points are available, whereas for $L_y = 12$, one cut hits directly the points $\pm \mathbf{Q}$ each. This is in line with the arguments given in [27]. Note that the minima in the dispersion at the corners of the Brillouin zone are not captured in the mean-field spinon theory. To resolve them in the variational Monte Carlo simulations, a Gutzwiller projection of the wave function is required [28].

G: Different Cylinder Geometries

The accessible momenta in the Brillouin zone also depend on the geometry of the cylinder, by which term we mean how to close the periodic circumference of the cylinder. Following the notation of Hu et al. [4], we define the geometry $YCL - n$ by the periodic translation vector $L \cdot \mathbf{a}_2 - n \cdot \mathbf{a}_1$. The standard way to close the periodicity that we chose for the simulations presented in this work is $YCL - 0 \equiv YCL$. The accessible parts of the Brillouin zone are shown in Fig. 10 for various L . Other possible geometries that come with a similar computational complexity for a given L since the resulting matrix product operator representing the Hamiltonian has comparable virtual bond dimensions are shown in Fig. 11. The $J_1 - J_2$ Heisenberg model on the triangular lattice for $L = 6$ as applied for the simulations in this work has for instance a virtual bond dimension of $\chi_{\text{MPO}} = 38$ if $J_2 \neq 0$. The advantage of the chosen geometry YCL , as apparent from Figs. 10 and 11, is that all high-symmetry momenta in the Brillouin zone such as the corners and the midpoints of the edges of the Brillouin zone are accessible.

* markus.drescher@tum.de

- [1] I. P. McCulloch, [arXiv:0804.2509](#) (2008).
- [2] M. P. Zaletel, R. S. K. Mong, C. Karrasch, J. E. Moore, and F. Pollmann, *Phys. Rev. B* **91**, 165112 (2015).
- [3] S. Paeckel, T. Köhler, A. Swoboda, S. R. Manmana, U. Schollwöck, and C. Hubig, *Annals of Physics* **411**, 167998 (2019).
- [4] S. Hu, W. Zhu, S. Eggert, and Y.-C. He, *Phys. Rev. Lett.* **123**, 207203 (2019).
- [5] S. Singh, R. N. C. Pfeifer, and G. Vidal, *Phys. Rev. A* **82**, 050301 (2010).
- [6] S. Singh, R. N. C. Pfeifer, and G. Vidal, *Phys. Rev. B* **83**, 115125 (2011).
- [7] J. Hauschild and F. Pollmann, *SciPost Phys. Lect. Notes* **5** (2018), 10.21468/SciPostPhysLectNotes.5.
- [8] Z. Zhu and S. R. White, *Phys. Rev. B* **92**, 041105 (2015).
- [9] W.-J. Hu, S.-S. Gong, W. Zhu, and D. N. Sheng, *Phys. Rev. B* **92**, 140403 (2015).
- [10] J. Haegeman, B. Pirvu, D. J. Weir, J. I. Cirac, T. J. Osborne, H. Verschelde, and F. Verstraete, *Phys. Rev. B* **85**, 100408 (2012).
- [11] L. Vanderstraeten, J. Haegeman, and F. Verstraete, *SciPost Phys. Lect. Notes* **7** (2019), 10.21468/SciPostPhysLectNotes.7.
- [12] M. Van Damme, R. Vanhove, J. Haegeman, F. Verstraete, and L. Vanderstraeten, *Phys. Rev. B* **104**, 115142 (2021).
- [13] T. Jolicoeur, E. Dagotto, E. Gagliano, and S. Bacci, *Phys. Rev. B* **42**, 4800 (1990).
- [14] A. V. Chubukov and T. Jolicoeur, *Phys. Rev. B* **46**, 11137 (1992).
- [15] J. Willsher, H.-K. Jin, and J. Knolle, *Phys. Rev. B* **107**, 064425 (2023).
- [16] R. Deutscher and H.-U. Everts, *Z. Physik B - Condensed Matter* **93**, 77 (1993).
- [17] A. E. Trumper, L. Capriotti, and S. Sorella, *Phys. Rev. B* **61**, 11529 (2000).
- [18] A. L. Chernyshev and M. E. Zhitomirsky, *Phys. Rev. Lett.* **97**, 207202 (2006).
- [19] O. A. Starykh, A. V. Chubukov, and A. G. Abanov, *Phys. Rev. B* **74**, 180403 (2006).
- [20] A. L. Chernyshev and M. E. Zhitomirsky, *Phys. Rev. B* **79**, 144416 (2009).
- [21] P. W. Anderson, *Phys. Rev.* **86**, 694 (1952).
- [22] R. Kubo, *Phys. Rev.* **87**, 568 (1952).
- [23] M. Hermele, T. Senthil, and M. P. A. Fisher, *Phys. Rev. B* **72**, 104404 (2005).
- [24] X.-Y. Song, C. Wang, A. Vishwanath, and Y.-C. He, *Nature Communications* **10**, 4254 (2019).
- [25] X.-Y. Song, Y.-C. He, A. Vishwanath, and C. Wang, *Phys. Rev. X* **10**, 011033 (2020).
- [26] Y. Shen, Y.-D. Li, H. Wo, Y. Li, S. Shen, B. Pan, Q. Wang, H. C. Walker, P. Steffens, M. Boehm, Y. Hao, D. L. Quintero-Castro, L. W. Harriger, M. D. Frontzek, L. Hao, S. Meng, Q. Zhang, G. Chen, and J. Zhao, *Nature* **540**, 559 (2016).
- [27] F. Ferrari, A. Parola, and F. Becca, *Phys. Rev. B* **103**, 195140 (2021).
- [28] F. Ferrari and F. Becca, *Phys. Rev. X* **9**, 031026 (2019).